Ann. Geophys., 34, 609–622, 2016
www.ann-geophys.net/34/609/2016/
doi:10.5194/angeo-34-609-2016

Annales Geophysicae Open Access EGU

Two-point observations of low-frequency waves at 67P/Churyumov-Gerasimenko during the descent of PHILAE: comparison of RPCMAG and ROMAP

Ingo Richter[1], Hans-Ulrich Auster[1], Gerhard Berghofer[2], Chris Carr[3], Emanuele Cupido[3], Karl-Heinz Fornaçon[1], Charlotte Goetz[1], Philip Heinisch[1], Christoph Koenders[1], Bernd Stoll[1], Bruce T. Tsurutani[4], Claire Vallat[5], Martin Volwerk[2], and Karl-Heinz Glassmeier[1]

[1]Institut für Geophysik und extraterrestrische Physik, TU Braunschweig, Mendelssohnstr. 3, 38106 Braunschweig, Germany
[2]Institut für Weltraumforschung, Schmiedlstraße 6, 8042 Graz, Austria
[3]Imperial College London, Exhibition Road, London SW7 2AZ, UK
[4]Jet Propulsion Laboratory, California Institute of Technology, 4800 Oak Grove Drive Pasadena, CA 91109, USA
[5]Rosetta Science Ground Segment, European Space Astronomy Centre, 28691 Villanueva de la Cañada, Madrid, Spain

Correspondence to: Ingo Richter (i.richter@tu-bs.de)

Received: 10 March 2016 – Revised: 23 June 2016 – Accepted: 28 June 2016 – Published: 14 July 2016

Abstract. The European Space Agency's spacecraft ROSETTA has reached its final destination, comet 67P/Churyumov-Gerasimenko. Whilst orbiting in the close vicinity of the nucleus the ROSETTA magnetometers detected a new type of low-frequency wave possibly generated by a cross-field current instability due to freshly ionized cometary water group particles. During separation, descent and landing of the lander PHILAE on comet 67P/Churyumov-Gerasimenko, we used the unique opportunity to perform combined measurements with the magnetometers onboard ROSETTA (RPCMAG) and its lander PHILAE (ROMAP). New details about the spatial distribution of wave properties along the connection line of the ROSETTA orbiter and the lander PHILAE are revealed. An estimation of the observed amplitude, phase and wavelength distribution will be presented as well as the measured dispersion relation, characterizing the new type of low-frequency waves. The propagation direction and polarization features will be discussed using the results of a minimum variance analysis. Thoughts about the size of the wave source will complete our study.

Keywords. Interplanetary physics (interplanetary magnetic fields) – space plasma physics (waves and instabilities) – space plasma physics (instruments and techniques)

1 Introduction

After a 10-year flight the ROSETTA spacecraft (Glassmeier et al., 2007a) arrived at its final target comet 67P/Churyumov-Gerasimenko (67P/C-G) in August 2014. At that time 67P/C-G was at a heliocentric distance of about 3.6 AU and its gas production rate was about $2 \times 10^{25}\,s^{-1}$ as reported by Gulkis et al. (2015). Neither any major plasma regions or boundaries were developed, nor a bowshock or a magnetic cavity formed at that time. Therefore, only plasma interactions of a weak comet as described by, e.g. Rubin et al. (2014) were expected in sharp contrast to the flybys at the more active comets 1P/Halley (Neubauer et al., 1986), 26P/Grigg-Skjellerup (Neubauer et al., 1993; Glassmeier and Neubauer, 1993), 21P/Giacobini-Zinner (Smith et al., 1986), and 19P/Borrelly (Richter et al., 2011).

Nevertheless the orbiter magnetometer RPCMAG observed magnetic, low-frequency waves with frequencies around 30–50 mHz and relative amplitudes up to about $\delta B/B \sim 1-2$ (Richter et al., 2015) almost continuously since ROSETTA had reached a distance of about 100 km to 67P/C-G in August 2014. These waves and their generation mechanism are clearly distinct from waves observed at other comets (Volwerk et al., 2014; Glassmeier et al., 1989).

In the months after arrival at 67P/C-G, ROSETTA operated under different conditions and at various distances to the comet. Thus, a comprehensive insight into the frequency and

amplitude characteristics of these waves may be gained. No information, however, could be retrieved on the wavelengths, velocities and the dispersion relation as only single-point observations were available. This situation changed during separation, descent (and rebound) and landing (SDL) of the ROSETTA lander PHILAE on 12 November 2014. During the 1.5 days of joint operations of the orbiter magnetometer RPCMAG (Glassmeier et al., 2007b) and the lander magnetometer ROMAP (Auster et al., 2007), wave observations at two different, spatially changing locations, were made which allow to deduce wavelength, velocity and propagation information as well.

In this paper we will give a short overview of the ROSETTA mission and the plasma instrumentation in Sect. 2. Section 3 includes the temporal and spatial evolution of wave properties and thus extends the findings presented in Richter et al. (2015) using also later observations. Particularly the energy density in a certain frequency band is a well-proven means to characterize wave properties and to compare wave observations made by different instruments at different locations. A detailed description of the SDL phase with its changing spacecraft separation distance and combined orbiter-lander observations, concentrating on the time interval between separation and landing of PHILAE, is presented in Sect. 4. Section 5 contains an example of a joint RPCMAG/ROMAP wave observation and an illustration of the high correlation of the detected waves. The frequency distribution of the waves will be analysed as well as the spatial separation dependence of the measured wave amplitudes. The extended treatment of our measurements including correlation techniques will lead us to the determination of the two point wave phase relations and the estimation of wavelengths. With knowledge of these parameters a dispersion relation of the observed waves can be determined. A minimum- and maximum-variance analysis reveals propagation properties.

As all measurements and analysis techniques are affected by certain errors a systematic error estimation is given in Sect. 6 in order to be able to draw the right conclusions in Sect. 7.

2 Mission overview and instrumentation

ESA's comet chaser mission ROSETTA (Glassmeier et al., 2007a) – launched in March 2004 – is designed for long-term cometary science studies in various scientific disciplines. After four planetary swingbys, two asteroid flybys, and a 2 and a half year hibernation period, ROSETTA was successfully turned on again in January 2014. After several innovative orbital manoeuvres it reached its target comet 67P/C-G on 6 August 2014 at a heliocentric distance of 3.6 AU. Unlike former cometary missions such as GIOTTO to comet 1P/Halley (Neubauer et al., 1986) and 26P/Grigg-Skjellerup (Neubauer et al., 1993; Glassmeier and Neubauer, 1993), ICE to 21P/Giacobini-Zinner (Smith et al., 1986) and DS1 to comet 19P/Borrelly (Richter et al., 2011) the Rosetta mission remained close to the comet nucleus ($\sim$ 10–250 km) for several months with relative velocities less than 1 m s^{-1}.

As not only observations in close vicinity of the target body but also measurements on the surface of 67P/C-G were intended to be conducted, the ROSETTA mission was designed to comprise two spacecraft: an orbiter observing the comet in varying distances between a few kilometres up to a few hundred kilometres, and the Lander PHILAE, performing measurements on the surface of 67P/C-G. PHILAE was successfully separated from the orbiter on 12 November 2014 at 08:35 UTC and performed its final landing at 17:31 UTC (Heinisch et al., 2016) after 9 h of descent. At the time of the landing 67P/C-G was at a heliocentric distance of 2.99 AU (Biele et al., 2015). The cometary activity over the August to November 2014 time period remained nearly constant, with a gas production rate of $\sim 1 \times 10^{26}$ s^{-1} (Bieler et al., 2015).

As ROSETTA is supposed to investigate plasma-physical properties in the surroundings and on the surface of 67P/C-G, it is equipped with two plasma packages, each of which containing a magnetometer experiment. The ROSETTA Plasma Consortium (RPC) (Carr et al., 2007) is a suite of five plasma sensors onboard the orbiter, and the ROMAP instrument (Auster et al., 2007) is a double-featured sensor comprising of a magnetometer and a plasma-monitor located on PHILAE.

The RPCMAG instrument, as part of RPC, is comprised of two triaxial fluxgate magnetometer sensors (FGM) (Glassmeier et al., 2007b) which are mounted on a 1.5 m long boom outside the orbiter, separated from each other by 15 cm. Due to this short boom, the small separation distance and a magnetically heavily polluted spacecraft, the magnetic field data were strongly disturbed by thrusters, transient currents, reaction wheel movements and heater currents. Therefore, removal of the time varying magnetic disturbance fields was a difficult task and data interpretation has to be conducted very carefully. RPCMAG can measure fields up to $\pm$16 000 nT with a resolution of 31 pT and a maximum sampling rate of 20 magnetic field vectors per second (burst mode).

The low-frequency waves, being the object of this study, occur in a frequency range ($\sim$ 20–50 mHz) where the contamination with spacecraft bias fields plays an insignificant role. We use RPCMAG data of the highest available calibration and cleaning level for our analyses: ground calibration results have been applied and furthermore the frequency dependent influence of ROSETTA's four rotating reaction wheels has been eliminated successfully. This was possible by knowledge of the wheel rotation frequencies which are provided as spacecraft-housekeeping parameters every 32 s. In the magnetic field raw data the wheel disturbance of $\sim$ 2 nT peak-to-peak amplitude occurred in the measurement baseband (0–10 Hz, mainly in the band above 1 Hz) as image frequencies of the original rotation frequencies (up to

1500 rpm) by multiple mirroring at the Nyquist frequency. The elimination was performed in the frequency domain by reducing the amplitude at the expected disturbance frequency down to the level of the surrounding spectral neighbourhood of the regarded data point. Calibration of the data and cleaning algorithms were employed to ensure that our analysis reveals real plasma effects and does not deal with spacecraft generated signatures.

The ROMAP magnetometer (Auster et al., 2007) onboard PHILAE is a single triaxial FGM sensor located on a 60 cm boom which was deployed roughly an hour after PHILAE was separated from the orbiter. ROMAP can measure fields up to ± 2000 nT with a resolution of 10 pT and a maximum sampling rate of 64 vectors per second. Due to operational constraints ROMAP had to be operated with the low vector rate of 1 Hz during SDL.

3 Evolution of wave activity deduced from long-term RPCMAG observations

The magnetometer is designed to be a low power consuming instrument which also generates only a small amount of telemetry packages. Therefore, RPCMAG has been allowed to operate almost continuously since spring 2014 while ROSETTA was still at about 1 million km away from the target comet. Thus, measurements spanning 1 year are available in order to study the new wave phenomena. All magnetic field observations described in this work are presented in the Cometary-centered Solar EQuatorial-coordinate system (CSEQ). Here the $+x$ axis points from the comet to the Sun, the $+z$ axis is the component of the Sun's north pole of date orthogonal to the $+x$ axis, and the $+y$ axis completes the right-handed reference frame. The origin of the coordinate system is the comet's centre of mass. All celestial-geometrical calculations were performed using the freely available, versatile SPICE software package (Acton, 1996). All errors given in this work are stated as error of the mean value, i.e. standard deviation divided by the square root of the number of datapoints.

Using the RPCMAG instrument we started to detect low-frequency waves at the beginning of August 2014 at a distance of ~ 100 km to 67P/C-G (Richter et al., 2015). In the meantime several months of successful operations were conducted allowing for a more detailed statistical analysis. Fig. 1 illustrates an example of well developed magnetic field waves observed by RPCMAG on 8 January 2015 between 22:00 and 22:15 UTC. The spacecraft was operating at a distance of ~ 27.5 km from the nucleus at that time. The shown waves are characterized by amplitudes of ~ 6 nT, a $\delta B/B \sim 1$, and frequencies of ~ 28 mHz. These amplitude and frequency values are typical for the newly detected low-frequency waves at 67P/C-G and first described by Richter et al. (2015).

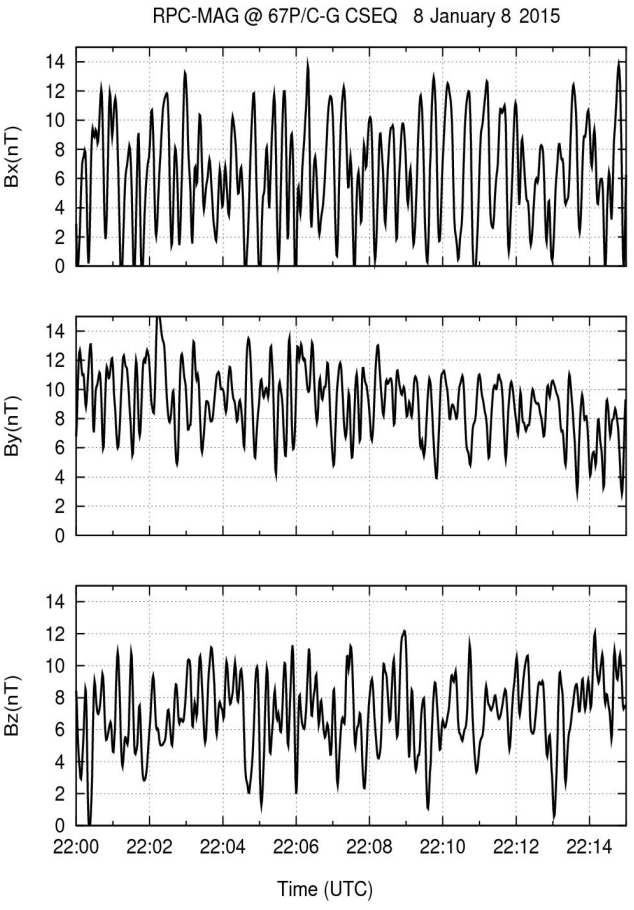

Figure 1. Magnetic field measurements made by RPCMAG on 8 January 2015, 22:00–22:15 UTC, as an example for the detection of low-frequency waves. Large-amplitude waves with a frequency of 28 mHz are clearly visible. The spacecraft position at that time was (0.2, −27, 5) km in the CSEQ-coordinate system.

In order to systematically investigate the temporal and spatial evolution of the wave activity, the energy density in the 10–100 mHz band has been calculated by integrating the power spectral density for almost 9000 hourly intervals. As a result Fig. 2 shows the radial dependence of the wave activity represented as the logarithm of the wave energy density as a function of spacecraft comet distance. The plot covers the first part of the ROSETTA's comet phase between May 2014 and April 2015 continuously.

As expected, measurements sampled from the solar wind over the time period of May–August 2014 (violet part) revealed very low and featureless energy density levels. However, the onset of wave activity at ~ 100 km altitude from the Comet's surface is associated with an abrupt increase of the energy density that persists up to the point that ROSETTA reached at a distance of 10 km in October 2014 (blue part).

Over the following months, between November 2014 and April 2015, ROSETTA moved again to larger distances (green part). However, as seen in Fig. 2, the energy density

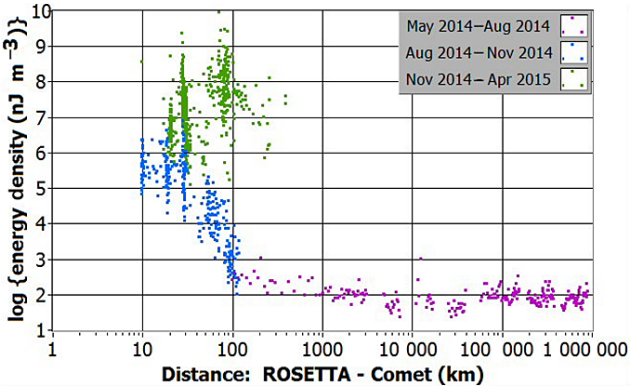

Figure 2. The energy density of the observed waves in dependence of the radial distance between ROSETTA and 67P/C-G for 1 year of observations. Time segments are colour-coded.

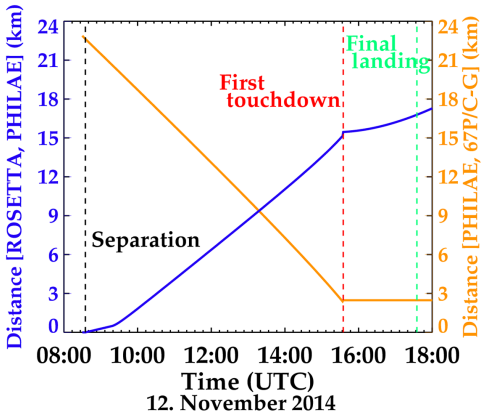

Figure 3. Temporal evolution of the distance between ROSETTA and PHILAE and also between PHILAE and 67P/C-G (centre) during the descent to 67P/C-G on 12 November 2014. The shown trajectories have been generated using the latest nominal kernels being available.

does not decrease again. This clearly indicates that wave activity strongly depends not only on radial distance to the nucleus but also on cometary activity which increased in the following months due to a decreasing comet-sun distance. A measure for the cometary activity is the gas production rate which increased by a factor of 3 from $1.5 \times 10^{26}\,\mathrm{s}^{-1}$ in November 2014 to $4.5 \times 10^{26}\,\mathrm{s}^{-1}$ in March 2015 according to K. C. Hansen (personal communication, 2015).

4 Joint RPCMAG–ROMAP observations

At 12 November 2014 – the day of landing – we had the unique opportunity of operating the two ROSETTA magnetometers in parallel at different locations. Thus, we use the descent phase of PHILAE to collect magnetic field data with both instruments, compare the waves detected with both sensors and analyse the relative wave phase shifts in order to estimate wavelength and wave velocity.

On 12 November 2014 at 08:35 UTC PHILAE separated from ROSETTA. This occurred at a distance of ~ 22.38 km from the comet (Biele et al., 2015). PHILAE veered away from the orbiter with a relative velocity of $\sim 0.7\,\mathrm{m\,s}^{-1}$. The temporal evolution of the radial distance between both spacecraft is shown in Fig. 3. The descent of PHILAE lasted for ~ 7 h, while its first touchdown occurred at 15:34 UTC at a distance of ~ 15 km from ROSETTA. PHILAE experienced two more ground contacts at 16:20 and 17:25 UTC before it settled in a fixed location on the comet's surface at 17:31 UTC (Auster et al., 2015). During PHILAE's journey, ROSETTA was slowly moving away from the comet.

Figure 4 exhibits the separation and descent scenario in more detail. The projected trajectories of both spacecraft including time-tags and the connecting lines between ROSETTA and PHILAE illustrate the spatio-temporal development of the spacecraft movements. During PHILAE's descent to 67P/C-G the distance between the vehicles increased continuously. The arc-like motion of PHILAE after 17:31 UTC is due to the common rotation with the comet.

A closer look at the direction of the shown imaginary lines connecting the two spacecraft reveals that these lines are approximately parallel over the time of descent. This important geometrical feature will be considered later during the estimation of the projected wavelength and the determination of the wave direction. In this context also the mean background field measured by RPCMAG shall be taken into account. It can be calculated by averaging the measured field over certain time intervals. From the background field point of view the descent phase can be split into three major time intervals showing three different field configurations:
$< \boldsymbol{B_0} >= (-5.5, -0.1, 4.6) \pm (0.02, 0.02, 0.02)$ nT
from 10:20 to 12:40 UTC,
$< \boldsymbol{B_0} >= (-3.6, -5.3, 7.9) \pm (0.02, 0.03, 0.02)$ nT
from 12:50 to 16:00 UTC and finally
$< \boldsymbol{B_0} >= (-0.3, -0.8, 0.4) \pm (0.03, 0.03, 0.03)$ nT
from 16:00 to 18:00 UTC. These values imply that the average angles between background field and the orbiter-lander connecting line changed as well and are given by $(154.5° \pm 0.3°)$, $(112.3° \pm 0.14°)$, $(98.0° \pm 1.85°)$ for the three time intervals. One can see that this angle follows a decreasing trend, meaning that the background field rotates against a direction perpendicular to the orbiter-lander connecting line. The average angle is roughly about 121°.

During SDL the orbiter magnetometer RPCMAG was permanently operating at 20 Hz sampling rate whereas the lander magnetometer ROMAP was operated at 1 Hz sampling rate. Due to this operational constraint the RPCMAG data had to be undersampled to an effective sample rate of 1 Hz in order to be directly comparable with ROMAP data. This reduction is done by just picking out every 20th raw vector

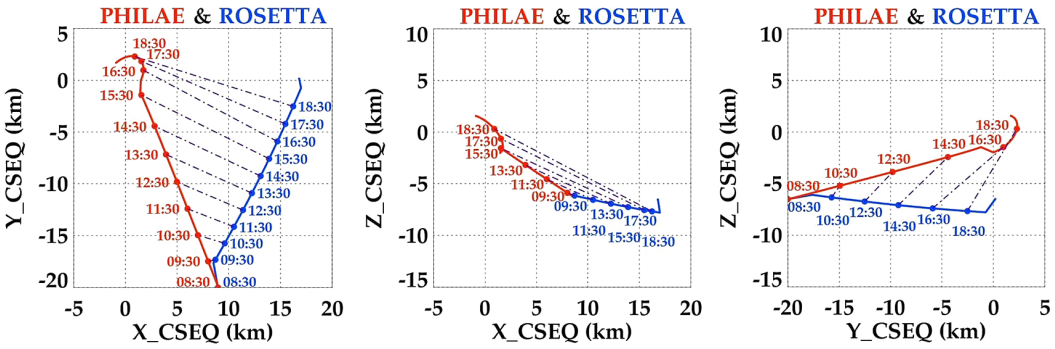

Figure 4. Projection of the two spacecraft trajectories in the xy-, xz-, and yz-planes of the CSEQ-system during the SDL phase. PHILAE's trajectory (red) and ROSETTA'S trajectory (blue) are shown including time-tags. The violet dash-dotted lines illustrate the orbiter-lander connecting lines at selected times. The data were derived from nominal SPICE kernels.

and resampling the data in order to be aligned to the ROMAP time tags.

To eliminate the effects imposed by internal spacecraft disturbance sources to the magnetic field data, a 1st order Butterworth-bandpass filter (Butterworth, 1930) was applied in the 10–100 mHz range. This technique allows us to concentrate in the frequency range of 20–50 mHz, which is the main interest of our analysis.

It should be noted that the lander attitude, i.e. the orientation of the Lander frame, in which the ROMAP data were measured, was primarily unknown during descent and landing as it could not be linked to any celestial coordinate system of reference. However, correlating RPCMAG and ROMAP data and rotating the ROMAP data to the RPCMAG system using a fit algorithm for minimizing the deviation of both datasets as described by Heinisch et al. (2016), allows for the determination of the lander attitude and the transformation of the ROMAP data to the CSEQ system as well. However, the attitude can not be calculated for all times during SDL, as on the one hand the correlation between RPCMAG and ROMAP is not high enough for certain intervals and on the other hand the complex rotation/nutation/precession of PHILAE precludes a proper derivation of geometrical parameters. Therefore, ROMAP data are available in a celestial linked coordinate system for selected intervals only. An impression of the manifold movement during descent can be received from the video sequence of the reconstructed flight (Heinisch and Finke, 2015). The available attitudes during descent and landing are in excellent agreement to OSIRIS[1] and CONSERT[2] observations (Sierks et al., 2015) as well as to the SONC[3] calculations (Jurado et al., 2016), giving us additional confidence that we have the correct orientations.

[1]Camera experiment onboard ROSETTA

[2]COmet Nucleus Sounding ExpeRimenT onboard ROSETTA & PHILAE

[3]Science and Operation Navigation Center, Toulouse,France

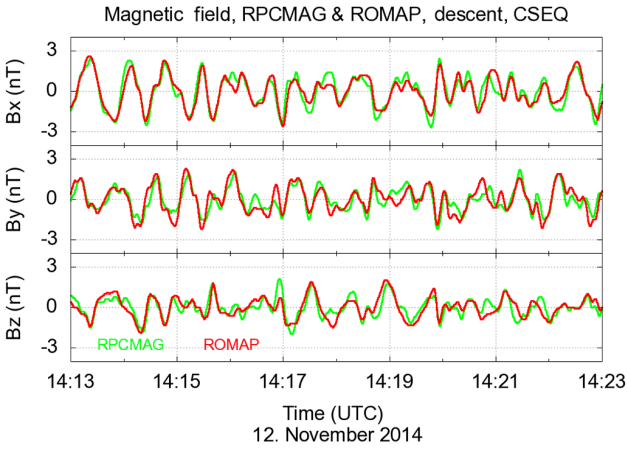

Figure 5. An example of 10 min parallel measurements of RPCMAG & ROMAP data during the PHILAE descent. Waves with frequencies of ∼ 30 mHz can clearly be seen in both time series.

5 Observational results

5.1 An example of joint magnetic field registration

Figure 5 shows a typical example of a processed magnetic field time series. Here all three magnetic field components measured by RPCMAG (green) and ROMAP (red) are displayed together within a 10 min interval on 12 November at 14:13–14:23 UTC. This interval illustrates the typical behaviour of the magnetic field during SDL. At this time the distance between PHILAE and ROSETTA was ∼ 11.5 km, and PHILAE was still ∼ 6.5 km away from the centre of 67P/C-G.

Waves with frequencies of ∼30 mHz can clearly be seen in both time series. The amplitudes of the waves at this time are roughly the same and the waves seen here are well-correlated, which means that the instruments are operating in the same plasma environment and scanning the same wave field.

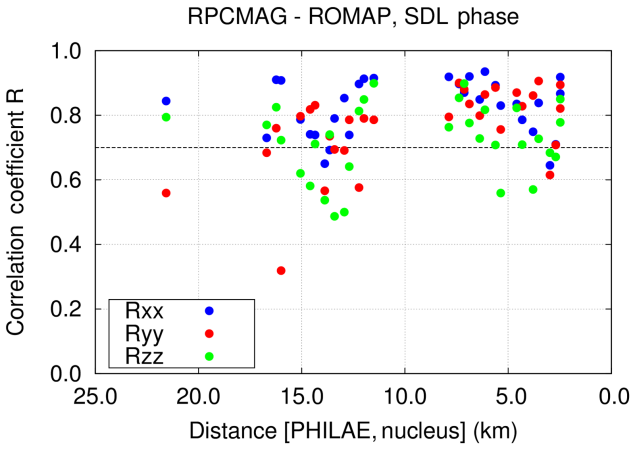

Figure 6. Correlation coefficients R_{xx} (blue), R_{yy} (red) and R_{zz} (green) of the six magnetic field components measured by RPCMAG and ROMAP. Correlation has been calculated using moving 300 s intervals and plotted versus the lander-comet distance. The horizontal line at $R = 0.7$ designates the usual lower confidence level.

5.2 Correlation of the observed waves

The magnetic field data of the 10 min time interval presented in Fig. 5 already indicates that magnetic measurements of both instruments are highly correlated during the SDL phase. A detailed correlation survey of pairwise analysed components from both instruments (B_x^{ROMAP}, B_x^{RPCMAG}), (B_y^{ROMAP}, B_y^{RPCMAG}), (B_z^{ROMAP}, B_z^{RPCMAG}) confirms their high degree of correlation (Fig. 6). The Pearson correlation coefficients R_{xx} (blue), R_{yy} (red) and R_{zz} (green) of the six magnetic field components are plotted versus the lander-comet distance, for all times, where data of both instruments are available. This analysis has been performed on moving, not overlapping 300 s intervals in order to investigate the datasets with a suitable granularity of time. Furthermore, the data have been shifted against each other in order to find the maximum correlation. The required shift of the individual intervals is in the order -2 ± 0.5 s without evidence of a unique pattern. The obtained results show that for 67 analysed intervals the correlation coefficients are above 0.7, while only 21 exhibit correlations below 0.7. This indicates that in 76 % of all cases where data are available, our separated instruments detected collective plasma structures and waves.

A rough estimate of the correlation length $l_c = \tau_c v$ can be calculated with knowledge of the coherence time τ_c and a typical propagation velocity v. The coherence time τ_c is the time lag for which the modulus of the normalized cross correlation function is decayed to $1/e$. From the analysis we obtain maximum coherence times of $\tau = 8$ s. A typical wave propagation velocity is the phase velocity v_p. As shown further down this is about $(6.1 \pm 0.8)\,\mathrm{km\,s^{-1}}$ in the present regime. Thus, the coherence length becomes roughly 48 km which is above the maximum orbiter-lander separation distance.

Predominantly high correlation coefficients between the waves observed with RPCMAG and ROMAP in all the visited areas allow us to draw conclusions about the plasma environment. Collective plasma oscillations occur on length-scales larger than the maximum orbiter-lander distance. Therefore, the wavelength of the observed waves must be also much larger than the maximum distance between orbiter and lander and thus any spatial aliasing effects do not play any role – otherwise the correlation coefficients (and the required time shift to obtain max. correlation) would show a significant spatial variation. Hence, we conclude from the correlation analysis that the wavelengths have to be larger than 18 km.

5.3 Frequency distribution of the observed waves

The frequency of the waves is one key characterization parameter, as it reflects the processes that the plasma undergo. For a dynamic frequency analysis within the complete descent and landing phase the magnetic field data have to be treated in a special way. As mentioned previously, first order Butterworth bandpasses with 10 and 100 mHz corner frequencies have been applied twice (forward and backward in time in order to avoid phase shifts). Furthermore the complete time series are split into chunks of 1200 s intervals which are shifted forward by 60 s in each step. Each of these intervals is cut into 300 s wide windows which is shifted by only half window widths, namely 150 s, in order to achieve a reasonable overlap and to perform a statistical significant frequency analysis. Thus, each 1200 s interval is divided into seven smaller intervals of 300 s, which are used to obtain averaged spectral information by summing up the individual results of the single windows. The chosen interval lengths turned out to be a suitable compromise between the low frequencies to be analysed and the fewer data points available during SDL.

For the proper assessment of the estimated frequencies three different types of frequencies are determined from the datasets: first ROMAP and RPCMAG time series are investigated separately and the two individual frequencies of the maximum wave power are calculated using dynamic power spectral analyses during the mentioned intervals above. In addition a cross-spectral analysis is executed using both datasets together and the frequencies of the maximum cross power is determined as well. The three resulting histograms of the calculated frequency distributions are presented in Fig. 7. The figure includes several interesting features: firstly, the observed frequency distributions for RPCMAG (green), ROMAP (red) and the maximum cross-power frequency (light-blue) show remarkable similarities. Secondly, there is no distinct single wave frequency but a broadband excitation in the 10–45 mHz range, not inconsistent with the (Richter et al., 2015) results that reported magnetic field oscillations

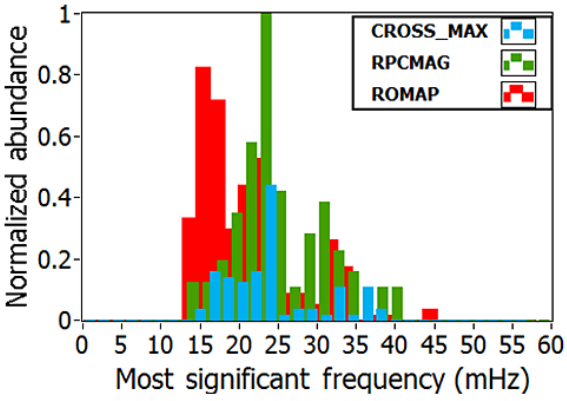

Figure 7. Normalized histograms (using 32 bins) of the most prominent frequencies for measurements by RPCMAG (green) and ROMAP (red). The flywheel signature of PHILAE at ∼ 15 mHz can clearly be identified. The blue histogram reflects the distribution of the frequencies at which the maximum cross power spectral density of both instrument datasets occurs.

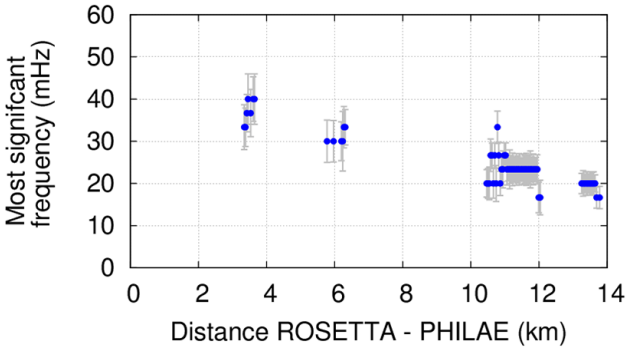

Figure 8. Profile of the most significant wave frequency (including gray error bars) versus the orbiter-lander distance. The frequency at which the cross-spectral density of RPCMAG and ROMAP measurements reaches its maximum value is plotted against the distance between ROSETTA and PHILAE during descent.

with a typical value of ∼ 40 mHz. However, the most dominant frequencies measured by *both* instruments in parallel are in the order of 25 mHz, as can be seen in the cross-power frequency distribution without a doubt. Third, the ROMAP data exhibit a much higher spectral content in the band around 15 mHz. The appearance of maximum power at these frequencies is due to the frequency aliasing signature of PHILAE's flywheels which are mirrored into this frequency band. This disturbance, however, could not be eliminated as the exact frequencies are not known due to a lack of lander housekeeping parameters at SDL. Hence, we conclude that the RPCMAG data and the signal in the undisturbed frequency band of the ROMAP data show a very similar frequency distribution. This is doubtlessly reflected in the distribution of the frequency of maximum cross-power. For the further analysis we concentrate purely on this frequency of max cross-power. Furthermore we only use time intervals where the correlation of both datasets is larger than $R = 0.75$, where the coherence is larger than 0.75 as well and where the cross power spectral density (rms) is larger than $2700\,\mathrm{nT^2\,Hz^{-1}}$ in order to select statistical significant intervals only.

Further information about the occurring frequencies of max cross-power is provided in Fig. 8. Here the spatial frequency distribution in dependency of the orbiter-lander distance is displayed. For times just after separation no observations are available, because the ROMAP boom was not deployed until 08:56 and ROMAP was therefore operating inside the ambient noise of PHILAE. Furthermore, the early phase of the descent was characterized by only low wave activity causing problems in determining PHILAE's attitude, as the attitude calculation – based on magnetic field measurements – is only possible if significant, collective magnetic variations are present.

Nevertheless the plot reveals an interesting pattern. There seems to be a trend showing that lower frequencies appear at larger ROSETTA-PHILAE distances. However, as these measurement were made at different times, a purely temporal dependency – or a dependency of any other changing plasma entity – could be causing this finding as well.

As described by Richter et al. (2015) the waves are assumed to be generated by a cross-field-current instability. As both the wave source as well as the two observing spacecraft are almost stationary in the nucleus rest frame (the velocities with respect to the CSEQ frame are in the order of $1\,\mathrm{m\,s^{-1}}$), any Doppler shift between wave transmitter and receiver, which usually has to be taken into account when discussing waves in the streaming solar wind, need not be considered here – the wave generator and the observer are located in the same frame. Furthermore, the interaction region is too small and the interaction time too short to accelerate the wave-carrying medium to significant velocities that might require Doppler shift considerations. It should be mentioned here as well that this short-term frequency distribution of the most prominent waves during SDL is similar to the one obtained by RPCMAG measurements made in the long-term comet observation phase between August 2014 and March 2015.

5.4 Amplitudes of the observed waves

For a detailed amplitude analysis the time series of RPCMAG and ROMAP data have been analysed in the frequency domain (Fig. 9). Shown are the amplitudes of the RPCMAG (green) and ROMAP (red) signals, derived from the power spectral density $P(f)$ as average over the three components (Amplitude $= \frac{1}{3}\sum_{i=x,y,z}\sqrt{P_i(f_{\max}) \times \Delta f}$, with $\Delta f = 1/T$ and T duration of the used data interval). The amplitudes represent again the waves at the frequencies of maximum cross power, displayed in spatial dependency of the orbiter-lander

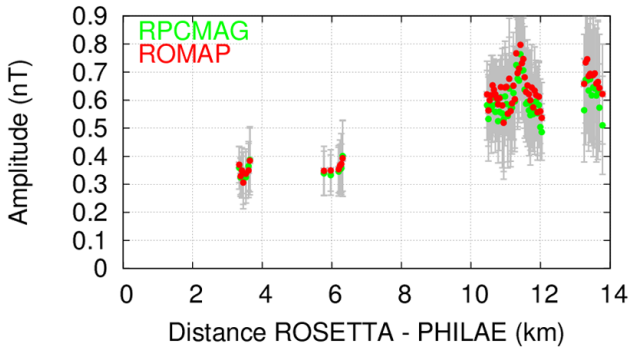

Figure 9. Amplitudes of magnetic fields observed by RPCMAG (green) and ROMAP (red) at the most significant frequencies plotted versus the orbiter-lander distance. The amplitudes represent the mean of all three components.

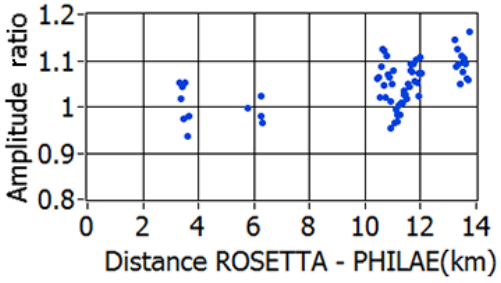

Figure 10. The ratio of the ROMAP/RPCMAG magnetic field amplitudes (from Fig. 9) plotted versus orbiter-lander distance.

distance. The 90 % confidence intervals of the amplitude determination are displayed in gray as error bars for both instruments. They have been computed according to standard procedure described in Bendat and Piersol (1971) (Sect. 4.4).

It can be seen that both instruments detect the same variations in the signals. Especially the common temporal variations registered at about 11 km distance prove spatial coherence of the observed plasma dynamics. This is consistent with the estimated coherence length of 48 km. In addition we know from the long-term observations that the "singing of the comet" commenced at 100 km distance from the comet. Therefore, we regard an area of ~ 100 km extension as an upper limit for the diameter of the source region of the observed waves.

Furthermore, it should be mentioned that the ROMAP signals were slightly larger for larger orbiter-lander distances compared with the RPCMAG amplitudes. This is exhibited even clearer in Fig. 10, where the ratio of the ROMAP/RPCMAG amplitudes is plotted versus the orbiter-lander distance. This ratio does not show an unambiguous amplitude change with varying orbiter-lander distance and lander-comet distance, as only fewer data and one descent profile are available. Nevertheless, the amplitudes in the vicinity of the comet seem to be up to ~ 10 % larger

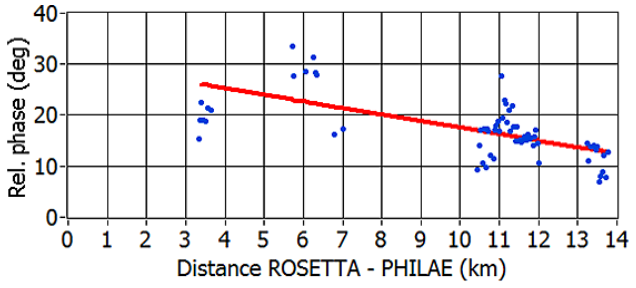

Figure 11. The phase shift between signals of RPCMAG and ROMAP (blue), taken at the frequency at which the maximum cross-spectral density occurs, versus the orbiter-lander distance. The red line represents the linear fit.

than farther away. The amplitude ratio ROMAP/RPCMAG at, e.g. 3.5 km orbiter-lander distance is about 1.0 ± 0.05. With increasing orbiter-lander distance, respectively decreasing lander-comet distance, the amplitude ratio rises continuously up to about 1.1 ± 0.05 at 13 km orbiter-lander distance. Despite the lack of multiple descent profiles available we tend to consider this increase as a significant change in amplitude ratio.

5.5 Phase relations and wavelength estimations

The relative phase shift of the waves measured at different locations is a key parameter for the estimation of the wavelength. This phase shift is calculated at the local frequency of maximum cross-power, derived from a cross-spectral analysis. The algorithm has been applied to all data available during the SDL segments using the parameters and thresholds mentioned above.

From the theoretical point of view the phase shift is identical for corresponding component-pairs $(B_x^{\mathrm{ROMAP}}, B_x^{\mathrm{RPCMAG}})$, $(B_y^{\mathrm{ROMAP}}, B_y^{\mathrm{RPCMAG}})$, and $(B_z^{\mathrm{ROMAP}}, B_z^{\mathrm{RPCMAG}})$. Therefore, the average of the phase shift $\Delta\varphi = \frac{1}{3}\sum_{i=x,y,z}\Delta\varphi_i$ will be used as the basis for the following considerations in order to derive a statistically significant result.

As a result of this phase analysis the relative phase shift $\Delta\varphi$ is plotted versus the orbiter-lander distance in Fig. 11. The phase shift is subject to certain spatio-temporal changes. For example at ~ 11 km distance an increased level of variation caused by temporal effects can be recognized, as already seen at the wave amplitude examination.

Due to the lack of scientifically usable data for the times where orbiter and lander were still connected (i.e. at 0 km distance) and where the ROMAP boom was still in its stowed positions, statements about phase shifts can only be made for ROSETTA/PHILAE distances between 3 and 14 km. From Fig. 11 a linear decrease of the relative phase shift can be derived as a rough estimate for this range. A spatial phase drop of $\Delta\varphi/\Delta r \approx (1.44° \pm 0.16°)/\mathrm{km}$ results. Here Δr de-

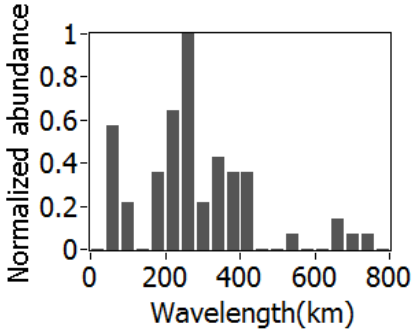

Figure 12. Normalized histogram (bin size: 40 km) of the estimated wavelengths, projected on the orbiter-lander connecting line.

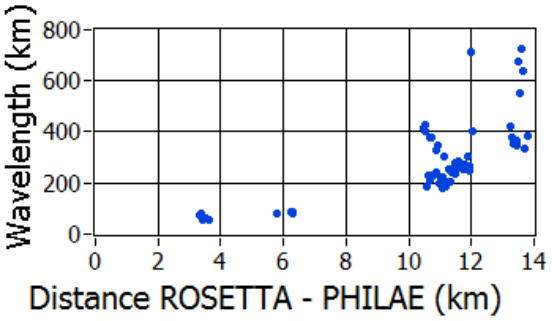

Figure 13. The estimated wavelengths, projected on the orbiter-lander connecting line, are plotted versus the orbiter-lander distance.

notes the orbiter-lander distance. The general phase relation of a wave is given by $\varphi = \omega t - k\,r$. Thus, the phase difference $\Delta\varphi = \varphi_2 - \varphi_1$ of two waves with equal angular frequencies ω is given by $\Delta\varphi = k \times \Delta r$.

It has to be noted for the following estimation of the wavenumber and wavelength that these entities have to be regarded as projected wavenumber k_p and projected wavelength λ_p onto the actual connecting line between orbiter and lander. As seen in Fig. 4 the direction of this connecting line is fairly constant during the descent. This means that this direction can be regarded as constant for the calculation and interpretation of the wavenumber and wavelength. Thus any occurring variation of the phase shift of the wave packets is subject to a varying distance between the points of observation and not to a changing direction of this baseline.

Thus, we get a projected wavenumber $k_\mathrm{p} = (\Delta\varphi/\Delta r) \times 2\pi/360^\circ = (2.5 \pm 0.28) \times 10^{-5}\,\mathrm{m}^{-1}$ from the measured phase decrease presented above. From this we calculate a projected wavelength $\lambda_\mathrm{p} = 2\pi/k_\mathrm{p} = (251 \pm 31)$ km.

A more detailed wavelength study can be performed using not only the global estimated phase gradient $\Delta\varphi/\Delta r$ but the actual phase shifts $\Delta\varphi_j$ at all possible distance Δr_j. This leads to a distribution of all calculated projected wavelengths $(\lambda_\mathrm{p})_j = (360^\circ/\Delta\varphi_j) \times \Delta r_j$, presented in the histogram in Fig. 12. It exhibits a broad distribution of a few hundred kilometres. with a calculated mean wavelength of $< \lambda_\mathrm{p} > = 278 \pm 19$ km as the most probable wavelength. The related mean wavenumber is $< k_\mathrm{p} > = (2.3 \pm 0.2) \times 10^{-5}\,\mathrm{m}^{-1}$. The computed wavelengths in dependency of the orbiter-lander distance are presented in Fig. 13.

The larger wavelengths and smaller wavenumbers, being exhibited at larger distances are related to lower frequencies at larger distances as can be seen in Fig. 8. This interrelationship suggests a systematical dispersion relation between k_p and ω being discussed now.

5.6 The dispersion relation

The combination of frequencies and wavelengths (respectively angular frequencies and wavenumber) in a common diagram, as exhibited in the plot of the calculated dispersion relation in Fig. 14, eliminates any direct spatio-temporal dependency discussed above, and reveals a statement about the wave velocities. From the observations (blue) we derive the angular frequency $\omega = 2\pi f$ and the related modulus of the projected wavenumber $k_\mathrm{p} = 2\pi/\lambda_\mathrm{p}$. As the angular frequency shows a linear behaviour with respect to the wavenumber, a linear fit (red) is added as well. The slope of the straight line, representing the group velocity $v_\mathrm{g} = \partial\omega/\partial k_\mathrm{p}$, has a constant value of $(1.2 \pm 0.3)\,\mathrm{km\,s}^{-1}$ (derived from a linear fit).

The phase velocity $v_\mathrm{p} = \omega/k$ varies with the wavenumber as the data are not represented by a straight line through the origin. For the most probable wavelength of $\lambda_\mathrm{p} = 278$ km a phase velocity $v_\mathrm{p} = 6.1\,\mathrm{km\,s}^{-1}$ results. For, e.g. $\lambda_\mathrm{p} = 500$ km we derive a phase velocity of $v_\mathrm{p} = 10.2\,\mathrm{km\,s}^{-1}$. These velocities are in the order of the values obtained from the plasma simulations in Koenders et al. (2016). For comparison the Alfvén-velocity computes as $v_\mathrm{A} = B_0/\sqrt{\mu_0\rho} = (2.23 \pm 0.47)\,\mathrm{km\,s}^{-1}$, under the assumption of an average background magnetic field of $B_0 = (5.3 \pm 0.1)$ nT, a mass density $\rho = n \times m_{\mathrm{H_2O}}$ of water ions, and a number density of $n \approx (150 \pm 30)\,\mathrm{cm}^{-3}$, taken as a rough estimate from RPCLAP measurements in October 2014 (Edberg et al., 2015). Thus, the Alfvén-velocity is in the same order of magnitude as the velocity of the "singing comet" waves.

5.7 Additional wave properties derived from variance analyses

Using the minimum- and maximum-variance analysis (MVA) additional wave properties have been obtained to complete the knowledge of the "singing comet" waves (Senfft, 2014). The analysis has been performed using moving windows of 300 s length with an overlap of 60 s for the complete SDL phase. RPCMAG and ROMAP datasets have been treated in the same way, only the flywheel disturbances at ∼ 15–18 mHz in ROMAP data have been damped using a bandpass with a lower corner frequency of 15 mHz

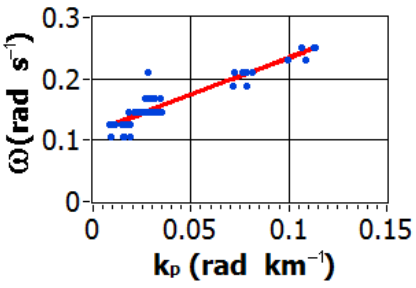

Figure 14. Derived dispersion relation (blue) including a linear fit (red). For the calculation the projected wavelength on the orbiter-lander connecting line and the related angular frequencies at which the maximum cross-power occurs have been used.

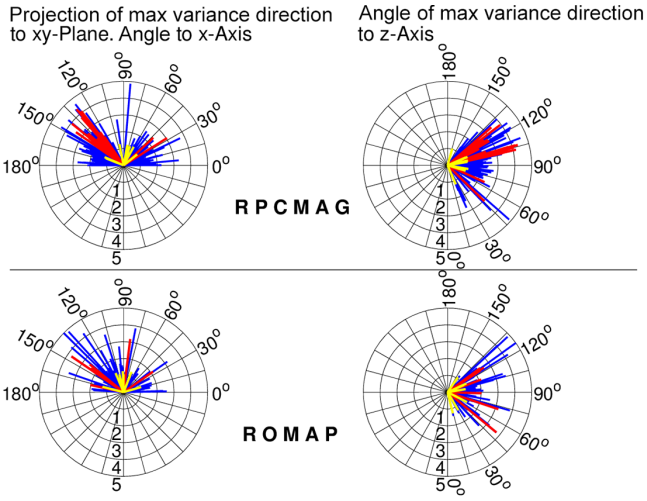

Figure 15. Distribution of *maximum* variance directions derived from RPCMAG (top) and ROMAP (bottom) data for the complete descent. Colour coding – blue: all MVA results, red: elliptical/more complex polarization ($\lambda_{max}/\lambda_{med} \geq 2$ and $\lambda_{med}/\lambda_{min} \geq 3$), yellow: circular polarization ($\lambda_{max}/\lambda_{med} \leq 1.3$ and $\lambda_{med}/\lambda_{min} \geq 3$). The radial component represents the eigenvalue ratios.

rather than 10 mHz as applied to the RPCMAG data. The resulting maximum variance directions are shown in Fig. 15, the minimum variance directions are plotted in Fig. 16. In both figures RPCMAG results are displayed in the top panels whereas ROMAP results are shown at the bottom. The azimuth represents the direction angle in degrees and the length of the lines visualizes the eigenvalue ratios. The plots are colour-coded in the following way: the blue lines represent the results of the complete MVA. The red lines mark elliptically or more complex polarized waves only, because the eigenvalue ratios for this subset are limited to $\lambda_{max}/\lambda_{med} \geq 2$ and $\lambda_{med}/\lambda_{min} \geq 3$. The yellow lines finally are related to circular polarized waves as the used eigenvalue ratios are confined by $\lambda_{max}/\lambda_{med} \leq 1.3$ and $\lambda_{med}/\lambda_{min} \geq 3$. The limiting ratio $\lambda_{med}/\lambda_{min} \geq 3$ has been chosen as a compromise in order to avoid any interpretation of misleading noise patterns and to keep an adequate amount of datapoints.

From the two columns of Fig. 15 qualitatively the same directions of maximum variance can be deduced in both planes. Due to less usable ROMAP observations the ROMAP results are more sparse. However, the common maximum variance direction is centered at $\sim \pm 45°$ around 90° to the CSEQ-z direction. This means the magnetic field oscillations mainly occur in the CSEQ-xy-plane. The left column of Fig. 15 shows the distribution of the projected variance direction in the CSEQ-xy plane with the x axis as a reference line. The blue pattern, representing results regardless of any eigenvalue constraints, is characterized by a quasi-homogeneous distribution, whereas the maximum variance of the elliptically or more complex polarized waves (red pattern) seems to have a weakly pronounced predominant direction at $\sim 140° \pm 10°$. Also circular waves (yellow), which are characterized by an eigenvalue ratio of $\lambda_{max}/\lambda_{med} \sim 1$, seem to be present. But as the amount of events is very low, they are not considered as a predominant phenomenon in this context.

The temporal behaviour of the maximum variance directions (not shown here), however, does not exhibit any striking feature, neither for ROMAP nor for the RPCMAG measurements.

The angle distribution of minimum variance directions, representing the wave propagation directions, can be obtained from Fig. 16. Also here a qualitative accordance between RPCMAG and ROMAP results can be seen. From RPCMAG we retrieve a projected angle of the most prominent elliptically or more complex polarized waves (red) onto the CSEQ-XY planes (left column) of about 20–40° and 200–220° (the MVA only yields directional information modulo ±180°). The analysis of ROMAP data yields a projected azimuth of about 165–180°. Thus, there is a directional deviation of $\sim 30°$ between both sets of observations. For the projected minimum variance direction onto the CSEQ-z axis (Fig. 16, right column) we find angles of about 105–120° for RPCMAG detected waves and about 30–45° for ROMAP observations. Considering that the angles are located on a cone-shaped shell around the z axis this results in a deviation of elevation between both datasets of roughly 20°.

From these findings we calculate (0.68, 0.44, 0.34) as the average minimum variance direction in the CSEQ-System. Only eigenvalue ratios of $\lambda_{med}/\lambda_{min} \geq 3$ have been used for this estimation.

This means that the main wave propagating direction during the descent points approximately in the diagonal in space direction from $+x+y+z$-Octant to the $-x-y-z$-Octant (or vice versa). Comparing this with the orbiter-lander connecting line shown in Fig. 4 we see that this direction is quasi perpendicular to the wave propagation direction. This explains why sometimes the wave-packets are seen first at ROMAP and sometimes first at RPCMAG.

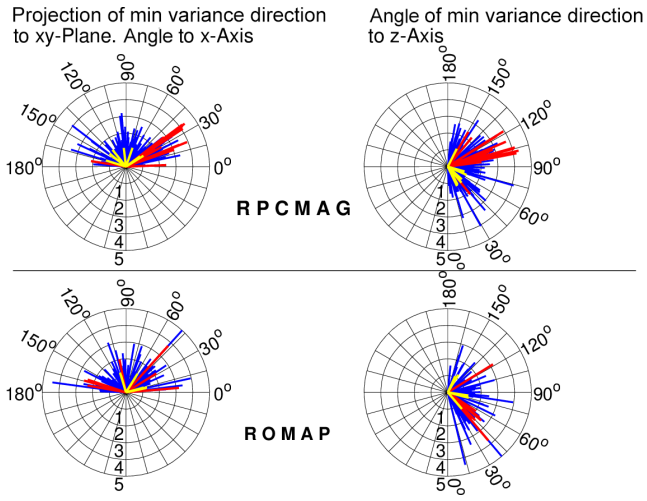

Figure 16. Distribution of *minimum* variance directions derived from RPCMAG (top) and ROMAP (bottom) data for the complete descent. Colour coding – blue: all MVA results, red: elliptical/more complex polarization ($\lambda_{max}/\lambda_{med} \geq 2$ and $\lambda_{med}/\lambda_{min} \geq 3$), yellow: circular polarization ($\lambda_{max}/\lambda_{med} \leq 1.3$ and $\lambda_{med}/\lambda_{min} \geq 3$). The radial component represents the eigenvalue ratios.

Furthermore the propagation direction can be compared with the mean direction of the background magnetic field. From the three major magnetic field configurations stated in the "joint observations section" we calculate the mean directions of the magnetic field as $< \boldsymbol{B_0}/B_0 >= (-0.77, -0.02, 0.64)$ for the interval 10:20–12:40 UTC, as $< \boldsymbol{B_0}/B_0 >= (-0.35, -0.52, 0.78)$ between 12:50 and 16:00 UTC and as $< \boldsymbol{B_0}/B_0 >= (-0.36, -0.82, 0.45)$ for the period 16:00–18:00 UTC. The conjunction of these findings with the results of the minimum variance analysis leads to angles between the mean magnetic field direction and the wave propagation direction of $(111° \pm 13°)$, $(69° \pm 10°)$, $(147° \pm 4°)$ for the three time intervals above. This means that the major wave propagation direction is roughly perpendicular to the main magnetic field direction.

The polarization analysis yields that elliptical or more complex modes are prevailing for all transversal waves showing a significant propagation direction defined by $\lambda_{med}/\lambda_{min} \geq 3$. The hodograms of these waves, however, do not show any prominent characteristics. There are neither purely left-handed not right-handed elliptical polarization patterns. Circular modes are present as well, but the amount of these events is too low to be able to extract reliable statements. Also the rotational sense of this polarization is highly variable and does not seem to follow any global principle.

6 Error estimation

As completion of the parameter discussion an error estimation shall be given finally. We are concentrating on wave properties only, therefore neither instrument offsets nor the s/c bias fields play any role. The influences of the orbiter reaction wheels have been eliminated, the disturbance of the lander fly wheels was recognized but does not influence the analyses as it is outside the frequency band of interest. Amplitudes and frequencies have been derived by the means of power spectral density analyses using moving time windows and averaging over sub-windows as described above. Thus, we have seven degrees of freedom in our spectral calculations, which is for sure not ideal, but a suitable compromise, in order to get a reasonable frequency resolution under the given circumstances.

The crucial point is the phase and wavelength calculation. For this the relative timing of both magnetometer datasets has to be precise. With our knowledge of the data handling onboard ROSETTA and PHILAE, we know that the timing accuracy is better than ± 1 s (conservative assessment). Translating this into a phase error at 25 mHz yields an uncertainty of $\pm 9°$. A calculation of the most probable wavelengths derived from distributions taking $\pm 9°$ phase offsets into account yields wavelengths of 223 and 313 km accordingly.

Furthermore, a conservative guess of the relative position error of 100 m would cause an additional uncertainty in wavelength of 1 % at 10 km distance.

As a final result we therefore obtain an assured value for projected wavelength in the order of about 300 km, derived from the joint RPCMAG/ROMAP measurements. This clearly proves the assumption made earlier that the considered region of observation is small in relation to the occurring wavelengths.

The considered phase error of $\pm 9°$ causes also an uncertainty in the derived wave velocities. The nominal group velocity of 1.2 km s^{-1} would vary between 1.1 and 1.4 km s^{-1} under the influence of the stated phase error.

A final remark on the variability of the obtained parameters shall be made here. During the considered descent and landing phase of PHILAE, which lasted about 9 h, the comet performed a 3/4-rotation. From long-term measurements it is known that, e.g. the outgassing rate, and also the particle density, is modulated not only with the comet rotation period but also with the half period of 6.2 h (Hässig et al., 2015). This means that also the close cometary environment is influenced by this variability. Furthermore, there is an asymmetry in outgassing between the Northern and Southern Hemisphere. Typical outflow velocities of the cometary neutrals are in the order of $\sim$1 km s^{-1} (as a snapshot measurement 0.68 km s^{-1} is reported by Gulkis et al., 2015). A typical velocity of the undisturbed solar wind is in the order of 400 km s^{-1}. It will be slowed down in the close vicinity of the comet due to ion pickup and mass-loading. All these processes vary on different spatial and temporal scales leading to variations seen in our separated observations and in the derived parameters.

The limitations originated in the equipment available has to be considered as well. We have only two spacecraft at

our disposal. Both are permanently moving, one is approaching a rotating comet with unknown properties. This situation complicates the interpretation of those results, which have to be derived from joint measurements, i.e. phase shifts, wavelengths and velocities. Hence the distinction between spatial and temporal effects stays ambiguous for these parameters. For proper determination of the real wavelength methods like the wave-telescope (Glassmeier et al., 2001) using four spacecraft would be needed, in order to remove the projection bias.

7 Conclusions

With the ROSETTA mission we were able to perform long-term magnetic field measurements during the long approach phase to 67P/C-G, and at 67P/C-G during landing of PHILAE. During SDL we had the unique opportunity to conduct a joint measurement with two magnetometers, RPCMAG and ROMAP, at different, varying locations. These joint measurements confirm the detection of low-frequency waves with frequencies around $\sim$ 20–50 mHz, amplitudes up to ~ 3 nT, and the estimated wavelength of Richter et al. (2015) in the order of a few hundred kilometres. Furthermore, we estimate an upper extension limit of the source region as about 100 km diameter and calculate the coherence length as roughly 48 km. Due to the small extension of the source region with respect to the wavelength we conclude that the wave source can be considered as quasi point-shaped.

The joint measurements also allowed to calculate the mean projected wavenumber ($< k_\mathrm{p} >= (2.3 \pm 0.2) \times 10^{-5}\,\mathrm{m}^{-1}$) and the dispersion relation – the relationship between observed pulsatances and wavenumbers. From this linear dispersion relation we were able to derive a constant group velocity $v_\mathrm{g} = (1.2 \pm 0.3)\,\mathrm{km\,s}^{-1}$ and the phase velocity $v_\mathrm{p} = (6.1 \pm 0.8)\,\mathrm{km\,s}^{-1}$ for a wave of 278 km wavelength.

According to the general antenna theory (Wheeler, 1959), the near field region of a radiator is located inside a sphere of $r_\mathrm{nf} = \lambda$, whereas the far field region is located at outside $r \gg 2\lambda$. This condition applies for short antennas with dimensions $D \leq \lambda/2$, whereas for larger antennas the border of near field region is given by the Fraunhofer length $r_\mathrm{f} = 2D^2/\lambda$. In the present case the extension of the source region is in the order of half of the wavelength. Thus, the transition region between near field and far field is somewhere between 71 and 278 km for a mean wavelength of 278 km. This implies that all observations during SDL were made in the near field region.

The dominating wave propagation direction can be found roughly along the diagonal in space direction from the CSEQ $(+x+y+z)$-Octant to the CSEQ $(-x-y-z)$-Octant (or vice versa, due to the MVA-ambiguity). Furthermore, the mean propagation direction of the low-frequency waves is roughly perpendicular to the local magnetic background field.

It has been demonstrated in Fig. 2 that the "singing comet" waves could be observed from August 2014 until March 2015, corresponding to heliocentric distances between 3.6 and 2.0 AU and to outgassing rates between $(1.5 - 4.5) \times 10^{26}\,\mathrm{s}^{-1}$ accordingly. Afterwards the waves vanished at still decreasing heliocentric distances. The perihelion at 1.3 AU was reached in August 2015. The waves reappeared finally in Spring 2016 at a distance of roughly 2.6 AU. A detailed long-term investigation of the temporal and spatial properties of the "singing comet" is not part of this work as we intentionally concentrated on the SDL phase. Such a study is, however, already in preparation by Goetz et al. (2016).

The comprehensive wave analysis presented in our work took advantage of the availability of the unique two point measurements during SDL, which were required to reveal the obtained wave properties.

We are heading to the end of the successful ROSETTA mission in September 2016, where final RPCMAG observations will be made along the planned and controlled descent of the ROSETTA orbiter down to 67P/C-G.

8 Data availability

The data used have been publictaed in the Planetary Science Archive (PSA) provided by ESA and the Planetary Data System (PDS) operated by NASA. PSA is accessible via: ftp://psa.esac.esa.int/pub/mirror/INTERNATIONAL-ROSETTA-MISSION/.

Used RPCMAG data can be found in the so called calibrated Prelanding-dataset:

RO-SS-RPCMAG-3-PRL-CALIBRATED-V6.0: Glassmeier, K.-H., Richter, I., Koenders, C., Goetz, C., Eichelberger, H., and Cupido, E.: ROSETTA RPCMAG PRELANDING PHASE (PRL) CALIBRATED DATA RECORD V6.0, RO-SS-RPCMAG-3-PRL-CALIBRATED-V6.0, ESA Planetary Science Archive and NASA Planetary Data System, 2016.

Used ROMAP data have been submitted to PSA but are still under review. They will be acessilbe in three different datasets:

RL-C-ROMAP-3-SDL-MAG-V1.0: Auster, H. U., Apathy, I., Berghofer, G., Remizov, A., and Roll, R.: ROSETTA-LANDER 67P ROMAP 3 SDL MAG V1.0, ESA Planetary Science Archive and NASA Planetary Data System, 2015.

RL-C-ROMAP-3-RBD-MAG-V1.0: Auster, H. U., Apathy, I., Berghofer, G., Remizov, A., and Roll, R.: ROSETTA-LANDER 67P ROMAP 3 RBD MAG V1.0, ESA Planetary Science Archive and NASA Planetary Data System, 2015.

RL-C-ROMAP-3-FSS-MAG-V1.0: Auster, H. U., Apathy, I., Berghofer, G., Remizov, A., and Roll, R.: ROSETTA-LANDER 67P ROMAP 3 FSS MAG V1.0, ESA Planetary Science Archive and NASA Planetary Data System, 2015.

Acknowledgements. The RPCMAG and ROMAP data will be made available through the PSA archive of ESA and the PDS archive of NASA. Rosetta is a European Space Agency (ESA) mission with contributions from its member states and the National Aeronautics and Space Administration (NASA). The work on RPCMAG and ROMAP was financially supported by the German Ministerium für Wirtschaft und Energie and the Deutsches Zentrum für Luft- und Raumfahrt under contract 50QP 1401. We thank the European taxpayers for the kind support of our space research. All computations concerning the s/c position and orientation have been calculated with use of the SPICE software developed by NASA's NAIF team. We thank K. C. Hansen for providing two values for the gas production rate which were extracted from a plot of a talk given at the ROSETTA SWT meeting at ESAC in December 2015. Portions of this research were performed at the Jet Propulsion Laboratory, California Institute of Technology under contract with NASA. We are indebted to the whole Rosetta Mission Team, SGS, and RMOC for their outstanding efforts making this mission possible. We express our sincere gratitude to the referees of this paper who contributed significantly to the finishing touch of this publication.

The topical editor, E. Roussos, thanks W.-H. Ip and one anonymous referee for help in evaluating this paper.

References

Acton, C. H.: Ancillary data services of NASA's navigation and ancillary information facility, Planet. Space Sci., 44, 65–70, doi:10.1016/0032-0633(95)00107-7, 1996.

Auster, H.-U., Apathy, I., Berghofer, G., Remizov, A., Roll, R., Fornacon, K.-H., Glassmeier, K.-H., Haerendel, G., Hejja, I., Kührt, E., Magnes, W., Moehlmann, D., Motschmann, U., Richter, I., Rosenbauer, H., Russell, C. T., Rustenbach, J., Sauer, K., Schwingenschuh, K., Szemerey, I., and Waesch, R.: ROMAP: ROSETTA Magnetometer and Plasma Monitor, Space Sci. Rev., 128, 221–240, doi:10.1007/s11214-006-9033-x, 2007.

Auster, H.-U., Apathy, I., Berghofer, G., Fornacon, K.-H., Remizov, A., Carr, C., Güttler, C., Haerendel, G., Heinisch, P., Hercik, D., Hilchenbach, M., Kührt, E., Magnes, W., Motschmann, U., Richter, I., Russell, C. T., Przyklenk, A., Schwingenschuh, K., Sierks, H., and Glassmeier, K.-H.: The nonmagnetic nucleus of comet 67P/Churyumov-Gerasimenko, Science, 349, doi:10.1126/science.aaa5102, 2015.

Bendat, J. and Piersol, A.: Random Data: Analysis and Measurement Procedures, WILEY-INTERSCIENCE, 1971.

Biele, J., Ulamec, S., Maibaum, M. , Roll, R., Witte, L. , Jurado, E., Muñoz, P., Arnold, W., Auster, H.-U., Casas, C., Faber, C., Fantinati, C., Finke, F., Fischer, H.-H., Geurts, K., Güttler, C., Heinisch, P., Herique, A., Hviid, S., Kargl, G., Knapmeyer, M., Knollenberg, J., Kofman, W., Kömle, N., Kührt, E., Lommatsch, V., Mottola, S., Pardo de Santayana, R., Remetean, E., Scholten, F., Seidensticker, K. J., Sierks, H., and Spohn, T.:The landing(s) of Philae and inferences about comet surface mechanical properties, Science, 349, doi:10.1126/science.aaa9816, 2015.

Bieler, A., Altwegg, K., Balsiger, H., Berthelier, J.-J., Calmonte, U., Combi, M., De Keyser, J., Fiethe, B., Fougere, N., Fuselier, S., Gasc, S., Gombosi, T., Hansen, K., Hässig, M., Huang, Z., Jäckel, A., Jia, X., Le Roy, L., Mall, U.A., Rème, H., Rubin, M., Tenishev, V., Tóth, G., Tzou, C.-Y., and Wurz, P.: Comparison of 3D kinetic and hydrodynamic models to ROSINA-COPS measurements of the neutral coma of 67P/Churyumov-Gerasimenko, A&A(583), A7, doi:10.1051/0004-6361/201526178, 2015.

Butterworth. S.: On the Theory of Filter Amplifiers, Wireless Engineer, 7, 536–541, 1930.

Carr, C., Cupido, E., Lee, C. G. Y., Balogh, A., Beek, T., Burch, J. L., Dunford, C. N., Eriksson, A. I., Gill, R., Glassmeier, K.-H., Goldstein, R., Lagoutte, D., Lundin, R., Lundin, K., Lybekk, B., Michau, J. L., Musmann, G., Nilsson, H., Pollock, C., Richter, I., and Trotignon, J. G.: RPC: The Rosetta Plasma Consortium, Space Sci. Rev., 128, 629–674, doi:10.1007/s11214-006-9136-4, 2007.

Edberg, N. J. T., Eriksson, A. I., Odelstad, E., Henri, P., Lebreton, J.-P., Gasc, S., Rubin, M., André, M., Gill, R., Johansson, E. P. G., Johansson, F., Vigren, E., Wahlund, J. E., Carr, C. M., Cupido, E., Glassmeier, K.-H., Goldstein, R., Koenders, C., Mandt, K., Nemeth, Z., Nilsson, H., Richter, I., Wieser, G. S., Szego, K., and Volwerk, M.: Spatial distribution of low-energy plasma around comet 67P/CG from Rosetta measurements, Geophys. Res. Lett., 42, 4263–4269, doi:10.1002/2015GL064233, 2015.

Glassmeier, K.-H. and Neubauer, F. M.: Low-Frequency Electromagnetic Plasma Waves at Comet P/Grigg-Skjellerup: Overview and Spectral Characteristics, J. Geophys. Res., 98, 20921–20935, doi:10.1029/93JA02583, 1993.

Glassmeier, K.-H., Coates, A.-J., Acuña, M.-H., Goldstein, M.-L., Johnstone, A.-D., and Neubauer, F.-M.: Spectral characteristics of low-frequency plasma turbulence upstream of Comet P/Halley, J. Geophys. Res., 94, 2156–2202, doi:10.1029/JA094iA01p00037, 1989.

Glassmeier, K.-H., Motschmann, U., Dunlop, M., Balogh, A., Acuña, M. H., Carr, C., Musmann, G., Fornaçon, K.-H., Schweda, K., Vogt, J., Georgescu, E., and Buchert, S.: Cluster as a wave telescope – first results from the fluxgate magnetometer, Ann. Geophys., 19, 1439–1447, doi:10.5194/angeo-19-1439-2001, 2001.

Glassmeier, K.-H., Boehnhardt, H., Koschny, D., Kührt, E., and Richter, I.: The Rosetta Mission: Flying Towards the Origin of the Solar System, Space Sci. Rev., 128, 1–21, doi:10.1007/s11214-006-9140-8, 2007a.

Glassmeier, K.-H., Richter, I., Diedrich, A., Musmann, G., Auster, U., Motschmann, U., Balogh, A., Carr, C., Cupido, E., Coates, A., Rother, M., Schwingenschuh, K., Szegö, K., and Tsurutani, B. T.: RPC-MAG The Fluxgate Magnetometer in the ROSETTA Plasma Consortium, Space Sci. Rev., 128, 649–670, doi:10.1007/s11214-006-9114-x, 2007b.

Goetz, C., Koenders, C., Heinisch P., Richter, I., Cupido, E., Carr, C., Vallat, C., and Glassmeier, K.-H.: Statistical Survey of Low-Frequency Waves in the Plasma Environment of Comet 67P/Churyumov-Gerasimenko, Astron. Astrophys., in preparation, 2016.

Gulkis, S., Allen, M., von Allmen, P., Beaudin, G., Biver, N., Bockelée-Morvan, D., Choukroun, M., Crovisier, J., Davidsson, B. J. R., Encrenaz, P., Encrenaz, T., Frerking, M., Hartogh, P., Hofstadter, M., Ip, W.-H., Janssen, M. Jarchow, C., Keihm, S., Lee, S., Lellouch, E., Leyrat, C., Rezac, L., Schloerb, F. P., and Spilker, T.: Subsurface properties and early activity of comet 67P/Churyumov-Gerasimenko, Science, 347, doi:10.1126/science.aaa0709, 2015.

Hässig, M., Altwegg , K., Balsiger, H., Bar-Nun, A., Berthelier, J. J., Bieler, A., Bochsler, P., Briois, C., Calmonte, U., Combi, M., De Keyser, J., Eberhardt, P., Fiethe, B., Fuselier, S. A., Galand, M., Gasc, S., Gombosi, T. I., Hansen, K. C., Jäckel, A., Keller, H. U., Kopp, E., Korth, A., Kührt, E., Le Roy, L., Mall, U., Marty, B., Mousis, O., Neefs, E., Owen, T., Rème, H., Rubin, M., Sémon, T., Tornow, C. , Tzou, C.-Y., Waite, J. H., Wurz, P.: Time variability and heterogeneity in the coma of 67P/Churyumov-Gerasimenko, Science, 347, doi:10.1126/science.aaa0276, 2015.

Heinisch, P. and Finke, F.: Reconstructing Philae's flight: Philae's two hour flight from Agilkia to Abydos, ESA, http://www.esa.int/spaceinvideos/Videos/2015/11/Reconstructing_Philae_s_flight (last access: 12 July 2016), 2015.

Heinisch, P., Auster, H.-U., Richter, I., Hercik, D., Jurado, E., Garmier, R., Güttler, C., and Glassmeier, K.-H.: Attitude-reconstruction of ROSETTA's lander PHILAE using two-point magnetic field observations by ROMAP and RPC-MAG, Acta Astronaut., 125, 174–182, doi:10.1016/j.actaastro.2015.12.002, 2016.

Koenders, C., Perschke, C., Glassmeier, K. H., Goetz, C., Richter, I., and Motschmann, U.: Low-Frequency Waves at Comet 67P/Churyumov-Gerasimenko: Observations Compared to Numerical Simulations, A&A, accepted, 2016.

Jurado, E., Martin, T., Canalias, E., Blazquez, A., Garmier, R., Ceolin, T., Gaudon, P., Delmas, C., Biele, J., Ulamec, S., Remetean, E., Torres, A., Laurent-Varin, J., Dolives, B., Herique, A., Roger, Y., Kofman, W., Jorda, L., Zakharov, V., Crifo, J.-F., Rodionov,A., Heinisch, P., and Vincent, J.-B.: Rosetta Lander Philae: Flight Dynamics analyses for Landing Site Selection and Post-Landing Operations, Acta Astronaut., 65–79, doi:10.1016/j.actaastro.2016.03.030, 2016.

Neubauer, F. M., Glassmeier, K.-H., Pohl, M., Raeder, J., Acuna, M. H., Burlaga, L. F., Ness, N. F., Musmann, G., Mariani, F., Wallis, M. K., Ungstrup, E., and Schmidt, H. U.: First results from the Giotto magnetometer experiment at comet Halley, Nature, 321, 352–355, doi:10.1038/321352a0, 1986.

Neubauer, F. M., Marschall, H., Pohl, M., Glassmeier, K.-H., Musmann, G., Mariani, F., Acuna, M. H., Burlaga, L. F., Ness, N. F., Wallis, M. K., Schmidt, H. U., and Ungstrup, E.: First results from the Giotto magnetometer experiment during the 26P/Grigg-Skjellerupencounter, Astron. Astrophys., 268(L5–L8), http://adsabs.harvard.edu/abs/1993A&A...268L...5N, 1993.

Richter, I., Koenders, C., Glassmeier, K.-H., Tsurutani, B. T., and Goldstein, R.: Deep Space 1 at comet 19P/Borrelly: Magnetic field and plasma observations, Planet. Space Sci., 59, 691–698, doi:10.1016/j.pss.2011.02.001, 2011.

Richter, I., Koenders, C., Auster, H.-U., Frühauff, D., Götz, C., Heinisch, P., Perschke, C., Motschmann, U., Stoll, B., Altwegg, K., Burch, J., Carr, C., Cupido, E., Eriksson, A., Henri, P., Goldstein, R., Lebreton, J.-P., Mokashi, P., Nemeth, Z., Nilsson, H., Rubin, M., Szegö, K., Tsurutani, B. T., Vallat, C., Volwerk, M., and Glassmeier, K.-H.: Observation of a new type of low-frequency waves at comet 67P/Churyumov-Gerasimenko, Ann. Geophys., 33, 1031–1036, doi:10.5194/angeo-33-1031-2015, 2015.

RL-C-ROMAP-3-SDL-MAG-V1.0: Auster, H. U., Apathy, I., Berghofer, G., Remizov, A., and Roll, R.: ROSETTA-LANDER 67P ROMAP 3 SDL MAG V1.0, ESA Planetary Science Archive and NASA Planetary Data System, 2015.

RL-C-ROMAP-3-RBD-MAG-V1.0: Auster, H. U., Apathy, I., Berghofer, G., Remizov, A., and Roll, R.: ROSETTA-LANDER 67P ROMAP 3 RBD MAG V1.0, ESA Planetary Science Archive and NASA Planetary Data System, 2015.

RL-C-ROMAP-3-FSS-MAG-V1.0: Auster, H. U., Apathy, I., Berghofer, G., Remizov, A., and Roll, R.: ROSETTA-LANDER 67P ROMAP 3 FSS MAG V1.0, ESA Planetary Science Archive and NASA Planetary Data System, 2015.

RO-SS-RPCMAG-3-PRL-CALIBRATED-V6.0: Glassmeier, K.-H., Richter, I., Koenders, C., Goetz, C., Eichelberger, H., and Cupido, E.: ROSETTA RPCMAG PRELANDING PHASE (PRL) CALIBRATED DATA RECORD V6.0, RO-SS-RPCMAG-3-PRL-CALIBRATED-V6.0, ESA Planetary Science Archive and NASA Planetary Data System, 2016.

Rubin, M., Koenders, C., Altwegg, K., Combi, M. R., Glassmeier, K.-H., Gombosi, T. I., Hansen, K. C., Motschmann, U., Richter, I., Tenishev, V. M., and Tóth, G.: Plasma environment of a weak comet – Predictions for Comet 67P/Churyumov–Gerasimenko from multifluid-MHD and Hybrid models, Icarus, 241, 38–49, doi:10.1016/j.icarus.2014.07.021, 2014.

Senfft, M.: Rosetta blog: The singing comet, ESA, available at: http://blogs.esa.int/rosetta/2014/11/11/the-singing-comet/ (last access: 12 July 2016), 2014.

Sierks, H., Guettler, C., and the OSIRIS Team: Rosetta news: Philae descent images, ESA, available at: http://www.esa.int/esatv/Videos/2015/05/Rosetta_news/Philae_descent_images, 2015.

Smith, E. J., Tsurutani, B. T., Slavin, J. A., Jones, D. E., Siscoe, G. L., and Asoka Mendis, D.: International cometary explorer encounter with Giacobini–Zinner: magnetic field observations, Science, 232, 382–385, 1986.

Volwerk, M., Glassmeier, K.-H., Delva, M., Schmid, D., Koenders, C., Richter, I., and Szegö, K.: A comparison between VEGA 1, 2 and Giotto flybys of comet 1P/Halley: implications for Rosetta, Ann. Geophys., 32, 1441–1453, doi:10.5194/angeo-32-1441-2014, 2014.

Wheeler, H. A.: The Radian Sphere Around a Small Antenna, 47, Proceedings of the IRE, Institute of Radio Engineers, 47, 1325–331, 1959.